
MUSA-PINN: Multi-scale Weak-form Physics-Informed Neural Networks for Fluid Flow in Complex Geometries

Weizheng Zhang^{*1} Xunjie Xie^{*1} Hao Pan² Xiaowei Duan¹ Bingteng Sun³ Qiang Du³ Lin lu¹

Abstract

While Physics-Informed Neural Networks (PINNs) offer a mesh-free approach to solving PDEs, standard point-wise residual minimization suffers from convergence pathologies in topologically complex domains like Triply Periodic Minimal Surfaces (TPMS). The locality bias of point-wise constraints fails to propagate global information through tortuous channels, causing unstable gradients and conservation violations. To address this, we propose the Multi-scale Weak-form PINN (MUSA-PINN), which reformulates PDE constraints as integral conservation laws over hierarchical spherical control volumes. We enforce continuity and momentum conservation via flux-balance residuals on control surfaces. Our method utilizes a three-scale subdomain strategy-comprising large volumes for long-range coupling, skeleton-aware meso-scale volumes aligned with transport pathways, and small volumes for local refinement-alongside a two-stage training schedule prioritizing continuity. Experiments on steady incompressible flow in TPMS geometries show MUSA-PINN outperforms state-of-the-art baselines, reducing relative errors by up to 93% and preserving mass conservation.

1. Introduction

Scientific machine learning has advanced rapidly in recent years, offering new paradigms for modeling and solving complex physical processes. Yet in engineering fluid dynamics, conventional computational fluid dynamics (CFD) remains the dominant tool (Slotnick et al., 2014; Versteeg, 2007), with costs that become prohibitive in parameterized design and optimization loops. High-efficiency heat exchangers exemplify this challenge: their performance relies

on geometrically intricate three-dimensional flow passages, and practical design exploration often requires repeated simulations across many geometric variations. Such simulations via CFD typically require high-quality volumetric meshes, but mesh generation for slender, tortuous, and topologically complex channels is time-consuming and frequently demands substantial expert effort and manual tuning (Hughes et al., 2005).

Physics-informed neural networks (PINNs) provide a mesh-free alternative by representing the solution field with neural networks and training with physics constraints from governing equations and boundary conditions (Raissi et al., 2019). PINNs are attractive for fast inference, differentiable modeling, and inverse problems with sparse observations (Karniadakis et al., 2021; Raissi et al., 2020). For high-dimensional fluid simulations, PINNs have the potential to significantly improve computational efficiency, in contrast to traditional CFD methods whose computational cost increases dramatically with problem dimensionality (Hwang, 2025). However, applying PINNs to industrial-grade internal flows with tortuous, high-aspect-ratio, and topologically complex channels remains challenging. Empirically, the accuracy and stability of standard PINNs often degrade substantially as geometric complexity increases, even for steady incompressible flows. Figure 1 provides a qualitative comparison of flow streamlines on an industrial liquid-cooling plate, contrasting CFD with a standard PINN baseline and MUSA-PINN. In this paper, we make the observation that a key reason for this failure is structural: the dominant training signal in standard PINNs is pointwise residual minimization, which cannot match with the global nature of conservation laws and produces a local-global inconsistency in complex transport geometries. In long and winding passages as found in heat exchangers, where information propagation along streamlines and across junctions is weak under purely local supervision, such locally small residuals frequently translate into physically inconsistent behavior.

A natural remedy to the above problem is to impose conservation in an integral sense. Prior attempts include enforcing global flux constraints between inlets and outlets (Hwang, 2025) or adopting variational formulations with element-wise quadrature (Kharazmi et al., 2021). Yet, global bound-

¹Shandong University, Qingdao, China ²Tsinghua University, Beijing, China ³Institute of Engineering Thermophysics, Chinese Academy of Sciences, Beijing, China. Correspondence to: Lin lu <llu@sdu.edu.cn>.

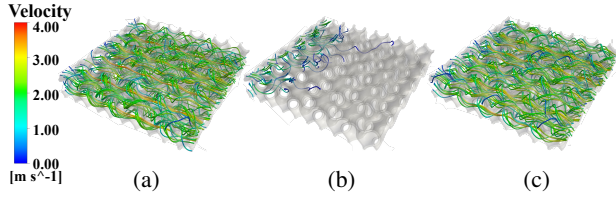


Figure 1. Flow streamlines on an industrial liquid-cooling plate. (a) CFD reference, (b) PINN-PE baseline (degrades in this complex geometry), and (c) MUSA-PINN. MUSA-PINN achieves a 14.91% relative ℓ_2 error in velocity w.r.t. CFD.

ary constraints are sparse and may leave the interior under-constrained, while element-based variational formulations typically require meshing and may introduce additional computational burdens or stability issues on complex geometries. This motivates a mesh-free formulation that enforces conservation over interior regions, so that physical information can propagate reliably through tortuous channels instead of being constrained only at scattered points or the outer boundary.

In this work, we propose MUlti-Scale weAk-form PINN (MUSA-PINN), a hybrid strong–weak form physics-informed framework for steady incompressible flow in complex geometries. Inspired by the classical Finite Element Analysis using weak form integral equations to improve convergence, our main idea is to reformulate governing equations into flux-balance constraints over control volumes using the Gauss divergence theorem, turning volumetric residuals into surface integrals of physically meaningful fluxes. These surface integrals are efficiently approximated by Monte Carlo sampling on control-volume boundaries, avoiding volumetric meshing while providing a more structured and globally informative training signal than pointwise residuals. To make the weak-form constraints effective across different industrial channels, we further introduce a multi-level subdomain placement strategy: large-scale control volumes encourage long-range conservation across transport pathways; medium-scale control volumes trace a geometry skeleton, so conservation signals follow flow channels; and small-scale control volumes refine local details and stabilize near-boundary behaviors. Together, these components provide dense conservation supervision throughout the domain and mitigate the local–global mismatch that limits conventional PINNs in complex internal flows.

We evaluate MUSA-PINN on flow channels extracted from Triply Periodic Minimal Surface (TPMS) structures, which serve as representative heat-exchanger passages due to their complex geometry and favorable transfer characteristics (Yerane & Rao, 2022). Experiments on multiple TPMS variants demonstrate that MUSA-PINN significantly improves solution accuracy and physical consistency over state-of-the-art baselines, and ablations verify the contributions

of the weak-form and multi-scale designs. We further discuss extensions toward more complex industrial components (e.g., liquid-cooling plates and DualMS channels (Zhang et al., 2025)) to highlight the scalability of the proposed approach.

Our main contributions are summarized as follows:

- Weak-form conservation via control volumes. We introduce a divergence-theorem-based formulation that enforces mass and momentum conservation through surface flux integrals over spherical control volumes, providing a volumetric mesh free and physically structured supervision signal beyond pointwise residuals.
- Multi-scale subdomain placement for complex channels. We design a multi-level strategy that improves coverage and information propagation in long, tortuous, and branching internal passages, bridging global consistency and local fidelity without manual domain decomposition.
- We benchmark on geometrically intricate TPMS heat-exchanger channels and conduct systematic comparisons and ablations, demonstrating consistent gains in accuracy and recovered flow structures, and outlining scalability to more complex industrial geometries.

2. Related Work

PINNs solve PDEs by parameterizing solution fields with neural networks and enforcing governing equations and boundary/initial conditions via automatic differentiation (Raissi et al., 2019; Cuomo et al., 2022). Recent studies have improved and analyzed PINNs training, including advances in architectures, optimization strategies, sampling schemes, and theoretical perspectives on when and why PINNs succeed or fail (Karniadakis et al., 2021; de la Mata et al., 2023; Toscano et al., 2025; Krishnapriyan et al., 2021). These developments position PINNs as a flexible learning-based solver family that can be deployed across diverse physical systems (Cai et al., 2021; Huang & Wang, 2022; Wang et al., 2023; Hu et al., 2024).

PINNs for Navier-Stokes equations. PINNs have been applied to incompressible Navier–Stokes flows under various settings, including data-scarce or label-free formulations and enhanced representations (Jin et al., 2021; Chen et al., 2021; Bai et al., 2020; Gao et al., 2021). While substantial progress has been demonstrated on many 2D benchmarks and simple 3D domains, steady flow prediction in 3D complex channels remains challenging due to intricate geometry, long-range coupling, and optimization instability. We target this regime and propose a weak-form, multi-scale formulation tailored to complex 3D geometries.

Strong-form PINNs and Weak-form PINNs. Strong-form PINNs minimize pointwise PDE residuals, offering a clean mesh-free pipeline but often exhibiting unstable optimization and weak global coupling in complex geometries. To mitigate these issues, many improvements have been proposed around adaptive sampling strategies (Lu et al., 2021; Zapf et al., 2022; Wu et al., 2023), dynamic loss reweighting (Wang et al., 2021a; 2022; Maddu et al., 2022), and training strategies (D. Jagtap & Em Karniadakis, 2020; Jagtap et al., 2020; Wang et al., 2024; 2025b), aiming to balance competing residual terms and stabilize convergence. Region-based approaches like RoPINN (Wu et al., 2024) mitigate local noise by averaging residuals over continuous neighborhoods, but remain strong-form that requires higher order differentiation. Furthermore, they rely on random sampling that ignores topological structures of local neighborhoods. Classical weak-form methods such as V-PINN (Kharazmi et al., 2019) offer rigorous reduction of differentiation order via variational principles but often reintroduce meshing overhead or subdomain partitioning (Kharazmi et al., 2021). We bridge these gaps with a Hessian-free integral formulation via the divergence theorem, and further place topology-guided control volumes along geometric skeletons to enforce flux conservation in a fully mesh-free manner.

Multi-scale PINNs. Existing multi-scale PINNs mainly address spectral bias or stiff coupling and can be grouped into three paradigms. Frequency-domain architectures combat spectral bias: MscaleDNN (Liu et al., 2020) employs frequency-scaled subnetworks to decompose target functions, while Fourier feature networks (Wang et al., 2021b) map coordinates into a Fourier embedding space. Optimization-centric strategies (e.g., Multi-Adam (Yao et al., 2023)) rebalance gradients across stiff loss terms via scale-invariant updates. Physical domain decomposition leverages physical priors to separate disparate spatio-temporal scales through reaction-rate grouping and boundary-layer/multiphysics decompositions (Weng & Zhou, 2022; Huang et al., 2024; Chaffart et al., 2024). However, they do not explicitly tackle the geometric spatial multi-scales in industrial complex domains, where flow hierarchy is governed by channel connectivity rather than frequency content or idealized priors. Our method targets this setting by enforcing integral conservation over multi-scale control volumes and placing them in a topology-aware fashion to propagate constraints along complex channels.

3. Methodology

We propose MUSA-PINN, a hybrid strong-weak physics-informed framework for steady incompressible flow in complex geometries (Figure 2). Starting from a standard strong-form PINN that minimizes pointwise Navier–Stokes residuals and boundary-condition violations, we additionally

impose weak-form conservation constraints over local integration subdomains. By integrating the governing equations over these subdomains and applying the divergence theorem, the weak constraints reduce to boundary flux-balance residuals that can be evaluated through surface integrals. To make the weak constraints effective and efficient on industrial-scale complex geometries, we further introduce a three-level multi-scale strategy to place integration subdomains at global, skeleton-aware, and local interior locations. This section first present the governing equations, then derives weak-form residuals, introduces the multi-scale subdomain construction, and finally presents the overall optimization objective.

3.1. Preliminaries

Problem Setting. We consider steady incompressible viscous flow in a complex three-dimensional geometry, a regime widely encountered in industrial internal-flow components (e.g., ducts and heat-exchanger passages) where the working fluid can often be treated as incompressible and a steady-state approximation is appropriate. Let $\Omega \subset \mathbb{R}^3$ denote the fluid domain and $\partial\Omega$ its boundary. We decompose the boundary into inlet, outlet, and wall parts:

$$\partial\Omega = \Gamma_{\text{in}} \cup \Gamma_{\text{out}} \cup \Gamma_{\text{w}}. \quad (1)$$

Nondimensional steady Navier–Stokes. We solve the nondimensional steady incompressible Navier–Stokes equations:

$$\begin{aligned} \nabla \cdot \mathbf{u} &= 0, & \text{in } \Omega, \\ (\mathbf{u} \cdot \nabla)\mathbf{u} + \nabla p - \frac{1}{Re} \nabla^2 \mathbf{u} &= \mathbf{0}, & \text{in } \Omega, \end{aligned} \quad (2)$$

where $\mathbf{u}(\mathbf{x}) \in \mathbb{R}^3$ and $p(\mathbf{x}) \in \mathbb{R}$ denote the velocity and pressure fields, respectively, and Re is the Reynolds number. The Reynolds number definition is given in Appendix A.1.

Boundary conditions. We enforce standard boundary conditions for internal flows: prescribed inlet velocity $\mathbf{u} = \mathbf{u}_{\text{in}}(\mathbf{x})$ on Γ_{in} , prescribed outlet pressure $p = p_{\text{out}}(\mathbf{x})$ on Γ_{out} , and no-slip walls $\mathbf{u} = \mathbf{0}$ on Γ_{w} .

PINN parameterization. We approximate the solution by a neural network $f_{\theta} : \mathbb{R}^3 \rightarrow \mathbb{R}^4$ that outputs

$$f_{\theta}(\mathbf{x}) = (\mathbf{u}_{\theta}(\mathbf{x}), p_{\theta}(\mathbf{x})), \quad (3)$$

where $\mathbf{u}_{\theta}(\mathbf{x}) \in \mathbb{R}^3$ and $p_{\theta}(\mathbf{x}) \in \mathbb{R}$ denote the predicted velocity and pressure fields, respectively. Let $\mathcal{X}_{\text{sf}} \subset \Omega$ be interior collocation points for enforcing the strong-form equations, and $\mathcal{X}_{\text{bc}} \subset \partial\Omega$ be boundary points for enforcing boundary conditions. The strong-form residuals at $\mathbf{x} \in \mathcal{X}_{\text{sf}}$

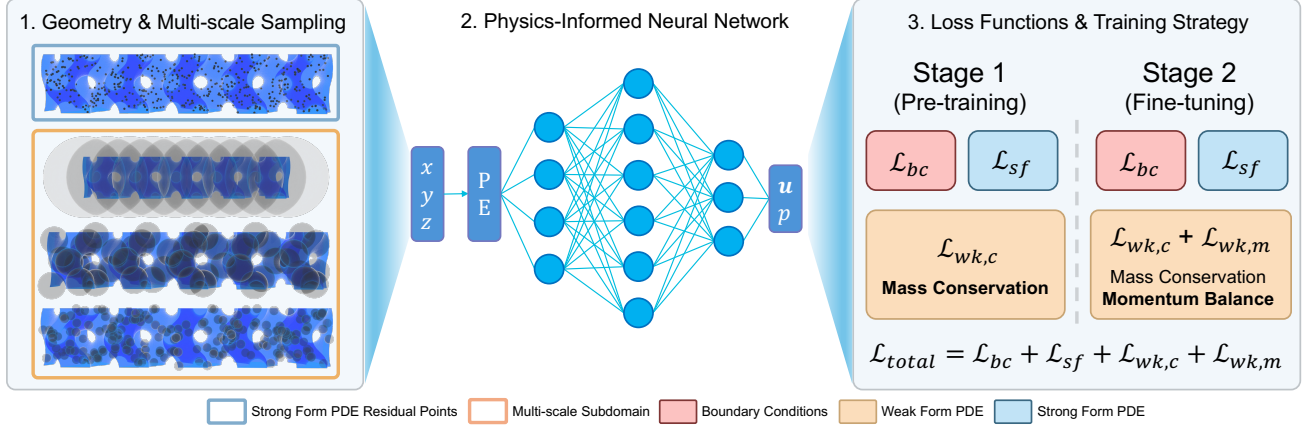


Figure 2. **MUSA-PINN pipeline.** We sample interior and boundary points for strong-form training and place multi-scale control volumes to impose weak conservation via surface fluxes. A coordinate-to-field MLP with positional encoding maps $(x, y, z) \mapsto (u, p)$ and is trained in two stages: Stage 1 uses $\mathcal{L}_{bc} + \mathcal{L}_{sf} + \mathcal{L}_{wk,c}$, and Stage 2 adds $\mathcal{L}_{wk,m}$, forming \mathcal{L}_{total} .

are defined as

$$\begin{aligned} r_c(\mathbf{x}) &:= \nabla \cdot \mathbf{u}_\theta(\mathbf{x}), \\ \mathbf{r}_m(\mathbf{x}) &:= (\mathbf{u}_\theta(\mathbf{x}) \cdot \nabla) \mathbf{u}_\theta(\mathbf{x}) + \nabla p_\theta(\mathbf{x}) - \frac{1}{Re} \nabla^2 \mathbf{u}_\theta(\mathbf{x}). \end{aligned} \quad (4)$$

These strong-form terms provide pointwise physics supervision and serve as baseline constraints in our hybrid objective.

3.2. Weak Formulation via Divergence Theorem

While the strong-form residuals enforce the PDE pointwise, they can be challenging to optimize on complex geometries. We therefore augment the strong-form PINN with weak-form conservation constraints defined over local integration subdomains. Importantly, our weak-form constraints are derived from the same strong-form Navier–Stokes equations and are imposed as additional supervision signals, rather than replacing the strong-form terms.

Local integration subdomains. For a center $\mathbf{c} \in \Omega$ and a radius $r > 0$, we define a spherical subdomain intersected with the fluid region:

$$V(\mathbf{c}, r) := B(\mathbf{c}, r) \cap \Omega, \quad (5)$$

where $B(\mathbf{c}, r) = \{\mathbf{x} \in \mathbb{R}^3 : \|\mathbf{x} - \mathbf{c}\| \leq r\}$. As illustrated in Figure 3, $\partial V(\mathbf{c}, r)$ decomposes into the spherical part and the clipped geometry part:

$$\partial V(\mathbf{c}, r) = (\partial B(\mathbf{c}, r) \cap \Omega) \cup (B(\mathbf{c}, r) \cap \partial \Omega), \quad (6)$$

corresponding to the spherical part and the clipped boundary part. Implementation details for constructing $V(\mathbf{c}, r)$ are provided in Appendix A.2.

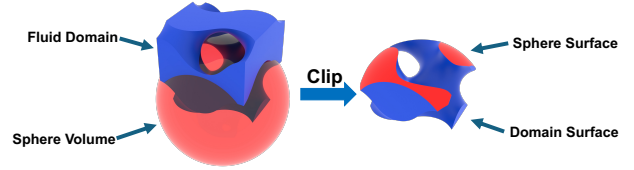


Figure 3. **Clipped integration subdomain.** A sphere $B(\mathbf{c}, r)$ (red) is intersected with the fluid domain Ω (blue) to form $V(\mathbf{c}, r)$.

Weak-form continuity constraint. Starting from $\nabla \cdot \mathbf{u} = 0$, integrating over $V(\mathbf{c}, r)$ and applying the divergence theorem yield

$$\int_{V(\mathbf{c}, r)} \nabla \cdot \mathbf{u} dV = \oint_{\partial V(\mathbf{c}, r)} \mathbf{u} \cdot \mathbf{n} dS = 0, \quad (7)$$

where \mathbf{n} denotes the outward unit normal on $\partial V(\mathbf{c}, r)$.

We define the weak-form continuity residual for the network prediction as

$$R_c(\mathbf{c}, r) := \oint_{\partial V(\mathbf{c}, r)} \mathbf{u}_\theta \cdot \mathbf{n} dS. \quad (8)$$

Weak-form momentum constraint. We rewrite the steady momentum equation in a divergence form. Using incompressibility, one practical nondimensional form is

$$\nabla \cdot (\mathbf{u} \otimes \mathbf{u}) + \nabla p - \frac{1}{Re} \nabla^2 \mathbf{u} = \mathbf{0}. \quad (9)$$

Noting that $\nabla^2 \mathbf{u} = \nabla \cdot (\nabla \mathbf{u})$, we obtain

$$\nabla \cdot \left(\mathbf{u} \otimes \mathbf{u} + p \mathbf{I} - \frac{1}{Re} \nabla \mathbf{u} \right) = \mathbf{0}. \quad (10)$$

Integrating over $V(\mathbf{c}, r)$ and applying the divergence theorem yield the boundary flux-balance condition

$$\oint_{\partial V(\mathbf{c}, r)} \left(\mathbf{u} \otimes \mathbf{u} + p \mathbf{I} - \frac{1}{Re} \nabla \mathbf{u} \right) \mathbf{n} dS = \mathbf{0}. \quad (11)$$

Accordingly, we define the weak-form momentum residual as

$$\mathbf{R}_m(\mathbf{c}, r) := \oint_{\partial V(\mathbf{c}, r)} \left(\mathbf{u}_\theta \otimes \mathbf{u}_\theta + p_\theta \mathbf{I} - \frac{1}{Re} \nabla \mathbf{u}_\theta \right) \mathbf{n} dS. \quad (12)$$

In practice, the surface integrals in Eq. (8) and Eq. (12) are evaluated by a volumetric mesh free Monte Carlo surface sampling scheme; details are provided in Appendix A.3.

3.3. Multi-scale Subdomain Placement Strategy

Industrial internal-flow geometries often exhibit challenging multi-scale characteristics, including long-range transport along slender passages, branching structures, and fine-scale geometric details. In such settings, weak-form constraints defined on a single scale can suffer from insufficient coverage or biased supervision: large subdomains emphasize global consistency but may miss local details, whereas small subdomains provide local refinement but may fail to propagate long-range conservation across the domain. To make weak-form enforcement both effective and efficient, we introduce a three-level multi-scale strategy that places integration subdomains at complementary locations and scales.

We consider three radii $r_L > r_M > r_S$ and construct three sets of subdomain centers, \mathcal{C}_L , \mathcal{C}_M , and \mathcal{C}_S . The radii are set from geometry-aware length scales, with details given in Appendix A.5. Each center $\mathbf{c} \in \mathcal{C}_s$ (with $s \in \{L, M, S\}$) defines an integration subdomain $V(\mathbf{c}, r_s) = B(\mathbf{c}, r_s) \cap \Omega$, on which the weak-form residuals in Eq. (8) and Eq. (12) are evaluated via the Monte Carlo estimator in Sec. 3.2.

Large-scale subdomains. We place large-radius subdomains to provide global coverage and enforce long-range conservation. Concretely, we sample centers \mathcal{C}_L throughout the geometry’s bounding box and keep those that lie inside Ω . These large subdomains couple distant regions through flux-balance constraints, stabilizing the global flow organization and reducing large-scale drift that may arise from purely pointwise supervision.

Medium-scale subdomains. To better cover slender and branching passages, we place medium-radius subdomains along the flow channel’s topological skeleton, as illustrated in Figure 4, which approximates the transport pathways inside Ω . Specifically, we extract a set of skeleton samples and use them as centers \mathcal{C}_M . This skeleton-aware placement yields contiguous weak-form coverage along the dominant flow routes and mitigates coverage holes that can occur with purely random interior sampling, especially in long tortuous channels and near junctions. We extract this skeleton using the Mean Curvature Flow algorithm (Tagliasacchi et al., 2012), which iteratively contracts the domain into a medial curve network. The resulting graph is then uniformly

sampled to define the final center positions \mathcal{C}_M .

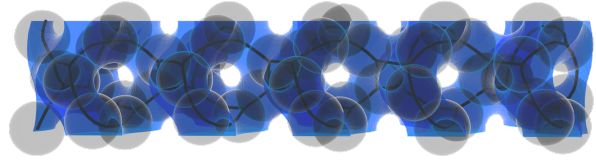


Figure 4. Medium-scale subdomains. These subdomains are centered along the skeletons (grey curves) of flow channels and have diameters that cover channel width.

Small-scale subdomains. Finally, we sample small-radius subdomains by drawing centers \mathcal{C}_S uniformly inside Ω . These local subdomains act as a refinement mechanism, strengthening weak-form supervision in regions with fine-scale geometric variations and helping reduce localized errors. Together with the large- and medium-scale sets, they provide dense local constraints without sacrificing global consistency.

The three scales play complementary roles: large subdomains encourage global consistency, skeleton-aware medium-scale subdomains ensure robust coverage along transport pathways, and small subdomains provide local refinement. In Sec. 3.4, we combine the weak-form losses aggregated over $\mathcal{C}_L, \mathcal{C}_M, \mathcal{C}_S$ with standard strong-form PINN losses to form the overall training objective.

3.4. Optimization Objective

Our training objective combines standard strong-form PINN losses with the multi-scale weak-form conservation losses. We minimize a weighted sum of interior PDE residuals, boundary-condition residuals, and weak-form flux balance residuals evaluated on the three-scale subdomain sets.

Strong-form loss. For interior collocation points \mathcal{X}_{sf} , we penalize the pointwise continuity and momentum residuals:

$$\mathcal{L}_{\text{sf}} = \frac{1}{|\mathcal{X}_{\text{sf}}|} \sum_{\mathbf{x} \in \mathcal{X}_{\text{sf}}} \left(\lambda_c |r_c(\mathbf{x})|^2 + \lambda_m \|\mathbf{r}_m(\mathbf{x})\|_2^2 \right), \quad (13)$$

where r_c and \mathbf{r}_m are defined in Eq. (4).

For boundary points $\mathcal{X}_{\text{bc}} \subset \partial\Omega$, we enforce inlet velocity, outlet pressure, and no-slip walls via

$$\mathcal{L}_{\text{bc}} = \lambda_{\text{in}} \mathcal{L}_{\text{in}} + \lambda_{\text{out}} \mathcal{L}_{\text{out}} + \lambda_{\text{w}} \mathcal{L}_{\text{w}}, \quad (14)$$

where \mathcal{L}_{in} , \mathcal{L}_{out} , and \mathcal{L}_{w} are mean-squared penalties on Γ_{in} , Γ_{out} , and Γ_{w} , respectively. The full expressions and the definitions of \mathcal{L}_{in} , \mathcal{L}_{out} , and \mathcal{L}_{w} are provided in Appendix A.6.

Multi-scale weak-form losses. For each scale $s \in \{L, M, S\}$ with radius r_s and centers \mathcal{C}_s , we define the

continuity and momentum weak residual losses:

$$\mathcal{L}_{\text{wk},c} = \sum_{s \in \{L,M,S\}} \lambda_c^s \frac{1}{|\mathcal{C}_s|} \sum_{\mathbf{c} \in \mathcal{C}_s} |R_c(\mathbf{c}, r_s)|^2, \quad (15)$$

$$\mathcal{L}_{\text{wk},m} = \sum_{s \in \{L,M,S\}} \lambda_m^s \frac{1}{|\mathcal{C}_s|} \sum_{\mathbf{c} \in \mathcal{C}_s} \|\mathbf{R}_m(\mathbf{c}, r_s)\|_2^2, \quad (16)$$

where R_c and \mathbf{R}_m are defined in Eq. (8) and Eq. (12) and evaluated via the Monte Carlo surface estimator (Appendix A.3).

Stage-gated overall objective. We minimize the following training objective:

$$\min_{\theta} \mathcal{L}(\theta; t) = \mathcal{L}_{\text{sf}} + \mathcal{L}_{\text{bc}} + \mathcal{L}_{\text{wk},c} + \gamma(t) \mathcal{L}_{\text{wk},m}, \quad (17)$$

where t is the training iteration and $\gamma(t)$ controls whether the weak-form momentum constraint is active. In our two-stage schedule, we set

$$\gamma(t) = \begin{cases} 0, & t < T_{\text{switch}} \quad (\text{Stage I: continuity warm-up}), \\ 1, & t \geq T_{\text{switch}} \quad (\text{Stage II: enable momentum}). \end{cases} \quad (18)$$

Stage I provides an integral incompressibility constraint that quickly suppresses long-range mass imbalance. Stage II activates the momentum flux-balance term, which further refines the flow field and improves physical consistency in complex passages. We choose T_{switch} as a fixed iteration or when $\mathcal{L}_{\text{wk},c}$ plateaus.

4. Experiments

4.1. Experimental Setup

Problem Setting. We evaluate the proposed MUSA-PINN on solving the 3D steady-state incompressible Navier-Stokes equations within four widely used high-efficiency TPMS-based heat-exchanger channels: **Primitive (P)**, **Gyroid (G)**, **Diamond (D)**, and **IWP**. These structures exhibit highly tortuous, interconnected pathways that induce complex secondary flows, posing severe challenges for numerical optimization. For each geometry, we tile one TPMS unit cell in a $1 \times 1 \times 5$ arrangement along the streamwise direction and consider the bounding box $\mathcal{D} = [0, 5] \times [0, 1] \times [0, 1]$, from which the fluid region $\Omega \subset \mathcal{D}$ is extracted (details in Appendix B.1). Ground truth solutions are generated using high-fidelity CFD simulations via Ansys CFX. Detailed solver configurations are provided in Appendix B.2.

Baselines. We benchmark our framework against conventional PINNs and three state-of-the-art physics-informed paradigms. To ensure a rigorous evaluation, we upgrade baselines with feature embeddings to mitigate spectral bias:

- (1) **PINN-PE**: Standard strong-form PINN with deterministic Fourier-feature positional encoding using linearly spaced frequencies; we found it more stable than random Fourier features (Tancik et al., 2020) in our setting (details in Appendix C).
- (2) **RoPINN** (Wu et al., 2024): A region-optimized approach that dynamically re-weights residuals based on local loss distributions.
- (3) **CoPINN** (Duan et al., 2025): A cognitive learning framework employing adaptive sampling strategies.
- (4) **MDPINN-GD** (Hwang, 2025): A multi-domain PINN that couples subdomains and enforces global dynamics constraints.

Implementation Details. We adopt a unified training protocol to enable fair comparisons. All paradigms use the same network architecture and SOAP optimizer (Wang et al., 2025a), with matched learning-rate schedules and loss weights, minimizing solver-induced confounders. Further details are given in Appendix C.

4.2. Comparative Analysis on Complex Geometries

Metrics. We report two complementary error measures for both velocity and pressure: mean squared error (MSE), and relative ℓ_2 error over the evaluation set in Table 1.

Performance Analysis. Across all methods, the Primitive (P) channel is comparatively easy: all baselines achieve low MSE and ℓ_2 errors, indicating that standard point-wise supervision can be sufficient when the geometry is less challenging. On the Gyroid (G) channel, the optimization becomes notably harder: among the baselines, only MDPINN-GD remains stable and produces non-degenerate solutions, while other point-wise methods frequently exhibit divergence or severe accuracy degradation. On the most challenging Diamond (D) and IWP channels, the gap becomes decisive. Most baselines collapse to physically inconsistent solutions, with relative errors exceeding 90% despite satisfying boundary conditions. In contrast, MUSA-PINN maintains stable convergence and achieves consistently low MSE and relative ℓ_2 errors across all four geometries. These results suggest that enforcing integral conservation on densely placed multi-scale control volumes provides a stronger interior supervision signal, which improves robustness in tortuous, highly connected passages where point-wise constraints struggle to propagate global physical consistency.

4.3. Analysis of Physical Consistency

To investigate the source of MUSA-PINN’s accuracy, we perform a detailed qualitative analysis focusing on global conservation and local field reconstruction.

Table 1. Quantitative comparison on TPMS channels. We report MSE and relative ℓ_2 error for velocity magnitude ($|\mathbf{u}|$) and pressure (p) across four geometries. **Bold** indicates the best performance, and underlined indicates the second best. **IMP.** denotes the relative improvement of MUSA-PINN over the best baseline for each metric.

Method	Ref	Primitive (P)				Gyroid (G)				Diamond (D)				IWP			
		$ \mathbf{u} $		p		$ \mathbf{u} $		p		$ \mathbf{u} $		p		$ \mathbf{u} $		p	
		MSE	ℓ_2	MSE	ℓ_2	MSE	ℓ_2	MSE	ℓ_2	MSE	ℓ_2	MSE	ℓ_2	MSE	ℓ_2	MSE	ℓ_2
PINN-PE	–	0.0006	3.76%	<u>0.0845</u>	<u>5.36%</u>	2.2042	83.19%	105.6067	86.21%	2.7627	90.18%	306.4535	83.04%	6.1360	94.49%	754.1458	101.69%
RoPINN	NeurIPS’ 2024	0.0005	3.51%	0.0948	5.67%	1.7492	74.11%	135.9094	97.80%	<u>2.5541</u>	<u>86.71%</u>	360.9349	90.12%	6.3375	96.45%	759.8746	102.07%
CoPINN	ICML’ 2025	0.0003	2.83%	0.1258	6.54%	2.1992	83.10%	105.5943	86.21%	2.7611	90.15%	306.4326	83.04%	6.1125	94.72%	752.9209	101.60%
MDPINN-GD	NeurIPS’ 2025	<u>0.0002</u>	<u>2.60%</u>	10.6390	60.01%	<u>0.6457</u>	<u>45.03%</u>	<u>14.5325</u>	<u>31.98%</u>	2.6693	88.64%	<u>300.3825</u>	<u>82.22%</u>	5.8951	<u>93.02%</u>	<u>686.5231</u>	<u>97.02%</u>
MUSA-PINN	Ours	0.0001	1.42%	0.0052	1.33%	0.0119	6.13%	2.3906	12.97%	0.0527	12.46%	31.3286	26.55%	0.0255	6.12%	96.4645	36.37%
IMP.	–	50%	45.38%	93.85%	75.19%	98.16%	86.39%	83.55%	59.44%	97.94%	85.63%	89.57%	67.71%	99.57%	93.42%	85.95%	62.51%

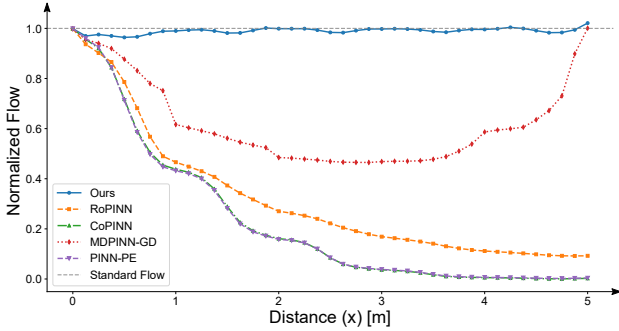


Figure 5. Evaluation of Global Mass Conservation. The plot shows the streamwise evolution of normalized mass flow rate $Q(x)/Q_{in}$ along the flow direction in the Gyroid structure. While standard methods exhibit significant mass leakage deviating from the theoretical value (gray line), MUSA-PINN maintains flux continuity, demonstrating the efficacy of volumetric constraints.

Table 2. Ablation on scale placement and weak-form schedule. We report relative ℓ_2 errors on velocity magnitude and pressure.

Variant	Rel. ℓ_2 on $ \mathbf{u} \downarrow$	Rel. ℓ_2 on $p \downarrow$
Large-only (C_L)	14.59%	87.41%
Medium-only (C_M)	87.72%	98.82%
Small-only (C_S)	89.99%	98.83%
Continuity-only ($\mathcal{L}_{wk,c}$)	13.28%	44.19%
Momentum-only ($\mathcal{L}_{wk,m}$)	95.87%	99.98%
Joint (no staging)	95.31%	99.98%
Full (ours, two-stage)	12.46%	26.55%

Global Mass Conservation. A critical failure mode of standard PINNs in long, winding channels is the violation of mass conservation due to error accumulation. We quantify this by measuring the mass flow rate mismatch $Q(x)/Q_{in}$ along the streamwise direction x in structure Gyroid, where $Q(x)$ is the cross-sectional volumetric flow rate at x and Q_{in} is its inlet value. As shown in Figure 5, baselines exhibit significant mass leakage within the domain. Although MDPINN-GD explicitly enforces flux balance at boundaries, it lacks dense internal constraints. MUSA-PINN, leveraged by large-scale integral constraints, effectively acts as a volumetric regularizer, enforcing strict flux continuity

throughout the entire domain. This results in a flow rate profile that tightly adheres to the conservation law, reducing the average cross-sectional mass error by over 97.05% compared to the best baseline.

Local Feature. Figure 6 visualizes the velocity magnitude slices in the high-curvature regions of the Gyroid structure. Baseline methods tend to produce over-smoothed solutions, failing to resolve the sharp velocity gradients near the surface boundaries. In contrast, MUSA-PINN utilizes multi-scale spherical constraints as dense, localized feature detectors. As highlighted in the zoomed-in views, our method successfully captures intricate secondary flows and boundary layer profiles that are washed out by baseline approaches, validating the capability of our weak-form formulation to preserve high-frequency physical details.

4.4. Ablation Studies

We ablate MUSA-PINN along two axes: *scale placement* and *weak-form design and schedule* in structure Diamond. For scale placement, we enable weak constraints on only one center set at a time: Large-only (C_L), Medium-only (C_M), and Small-only (C_S). For weak-form design and schedule, we use the full multi-scale placement but vary the enforced laws and schedule: Continuity-only, Momentum-only, Joint (no staging)(continuity+momentum from the start), and Full (ours) (two-stage: continuity warm-up then enable momentum). Table 2 shows that the velocity magnitude of single-scale variants are consistently inferior, and the two-stage schedule is more stable and accurate than training continuity and momentum jointly from scratch.

4.5. Performance on More Challenging Regimes

We further stress-test MUSA-PINN under harder physics and geometries to evaluate robustness at higher Reynolds numbers, applicability to industrial components, and empirical capacity scaling.

Higher-Reynolds-number Gyroid. We evaluate Gyroid at $Re \in \{200, 400\}$, where stronger inertial effects typically make PINN training more fragile. MUSA-PINN remains

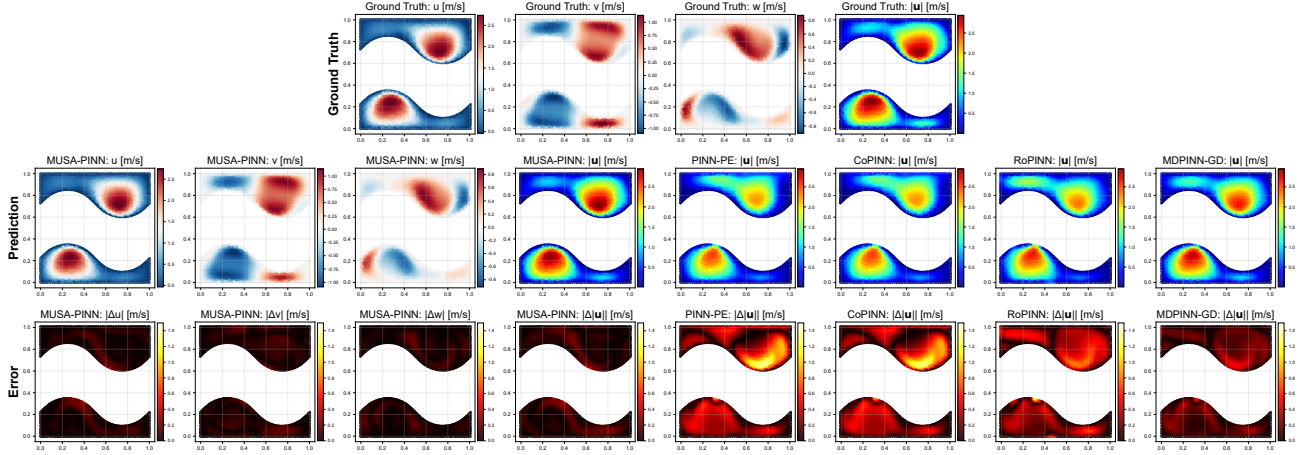


Figure 6. Qualitative comparison of velocity predictions on the Gyroid slice at $x = 0.5$. MUSA-PINN better preserves the component-wise flow structures and yields consistently lower absolute errors than the baselines. More details are provided in Appendix D.1 and D.2.

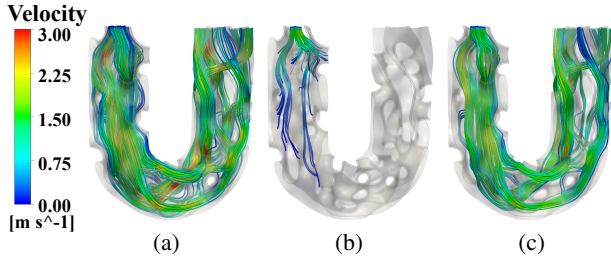


Figure 7. Flow streamlines on DualMS heat exchanger. (a) CFD reference, (b) PINN-PE baseline (degrades in this complex geometry), and (c) MUSA-PINN. MUSA-PINN achieves a 20.08% relative ℓ_2 error in velocity w.r.t. CFD.

Table 3. Empirical capacity scaling on the liquid cooling plate. Relative ℓ_2 errors of MUSA-PINN with different MLP capacities under the same training protocol. Width \times depth denotes (hidden units per layer) \times (number of hidden layers).

Model	Width \times Depth	#Params	$ u $ Rel. $\ell_2 \downarrow$	p Rel. $\ell_2 \downarrow$
MUSA-PINN	256×5	280K	14.91%	23.49%
MUSA-PINN	256×8	477K	14.18%	11.49%
MUSA-PINN	512×5	1084K	13.82%	20.83%

stable and achieves relative ℓ_2 errors of 14.27%/21.08% for $|u|$ and 4.26%/8.09% for p at $Re = 200/400$, respectively.

Industrial geometries: liquid cooling plate and DualMS heat exchanger. We further test MUSA-PINN on a liquid cooling plate and a DualMS channel to assess robustness on industrial-scale complex geometries. Figures 1, 7 visualizes the flow streamlines of industrial geometries, and the relative ℓ_2 errors against CFD are reported in the caption. Note the discontinuity in the standard PINN streamlines vs. the smooth flow in MUSA-PINN.

Empirical capacity scaling. We keep the training protocol fixed and vary the MLP width and depth to study capacity effects on the liquid cooling plate. Table 3 shows a consistent decrease in relative ℓ_2 error as capacity increases, indicating that larger networks yield more accurate solutions in this industrial-scale geometry.

5. Discussion and Conclusion

In this paper, we presented MUSA-PINN, a novel multi-scale weak-form framework designed to tackle the optimization pathologies of Navier-Stokes equations in topologically complex geometries. By enforcing integral conservation on hierarchically placed control volumes, MUSA-PINN strengthens long-range physical coupling while preserving local fidelity, alleviating the local–global mismatch that often hinders pointwise PINN training. Across TPMS heat-exchanger channels, MUSA-PINN consistently improves accuracy and physical consistency over competitive baselines. We further validate its effectiveness on more realistic internal-flow geometries, including cold-plate and DualMS channels, demonstrating its potential as a scalable volumetric mesh free surrogate for component-level flow simulation.

Limitations. MUSA-PINN incurs additional training cost due to integration on spherical control-volume surfaces, training time details in Appendix D.3. Moreover, the current control-volume placement is heuristic; learning task-adaptive constraint placement remains an open problem.

Future Work. We identify two key extensions for MUSA-PINN. First, we will adapt the framework to transient regimes by constructing spatiotemporal control volumes to enforce conservation over time. Second, we will incorporate energy equations to model conjugate heat transfer, enabling a unified multiphysics framework for end-to-end heat-exchanger optimization.

Impact Statement

This paper presents work whose goal is to advance the field of machine learning. There are many potential societal consequences of our work, none of which we feel must be specifically highlighted here.

References

- Bai, X.-d., Wang, Y., and Zhang, W. Applying physics informed neural network for flow data assimilation. *Journal of Hydrodynamics*, 32(6):1050–1058, December 2020. ISSN 1878-0342. doi: 10.1007/s42241-020-0077-2. URL <http://dx.doi.org/10.1007/s42241-020-0077-2>.
- Cai, S., Mao, Z., Wang, Z., Yin, M., and Karniadakis, G. E. Physics-informed neural networks (pinns) for fluid mechanics: A review. *Acta Mechanica Sinica*, 37(12):1727–1738, 2021.
- Chaffart, D., Yuan, Y., and Ricardez-Sandoval, L. A. Multiscale physics-informed neural network framework to capture stochastic thin-film deposition. *The Journal of Physical Chemistry C*, 128(9):3733–3750, February 2024. ISSN 1932-7455. doi: 10.1021/acs.jpcc.3c07168.
- Chen, Z., Liu, Y., and Sun, H. Physics-informed learning of governing equations from scarce data. *Nature Communications*, 12(1), October 2021. ISSN 2041-1723. doi: 10.1038/s41467-021-26434-1. URL <http://dx.doi.org/10.1038/s41467-021-26434-1>.
- Cuomo, S., Di Cola, V. S., Giampaolo, F., Rozza, G., Raissi, M., and Piccialli, F. Scientific machine learning through physics-informed neural networks: Where we are and what’s next. *Journal of Scientific Computing*, 92(3):88, 2022.
- D. Jagtap, A. and Em Karniadakis, G. Extended physics-informed neural networks (xpinn): A generalized space-time domain decomposition based deep learning framework for nonlinear partial differential equations. *Communications in Computational Physics*, 28(5):2002–2041, June 2020. ISSN 1991-7120. doi: 10.4208/cicp.oa-2020-0164.
- de la Mata, F. F., Gijón, A., Molina-Solana, M., and Gómez-Romero, J. Physics-informed neural networks for data-driven simulation: Advantages, limitations, and opportunities. *Physica A: Statistical Mechanics and its Applications*, 610:128415, 2023.
- Duan, S., Wu, W., Hu, P., Ren, Z., Peng, D., and Sun, Y. CoPINN: Cognitive physics-informed neural networks. In *Forty-second International Conference on Machine Learning*, 2025. URL <https://openreview.net/forum?id=4vAa0A98xI>.
- Gao, H., Sun, L., and Wang, J.-X. Phygeonet: Physics-informed geometry-adaptive convolutional neural networks for solving parameterized steady-state pdes on irregular domain. *Journal of Computational Physics*, 428:110079, March 2021. ISSN 0021-9991. doi: 10.1016/j.jcp.2020.110079. URL <http://dx.doi.org/10.1016/j.jcp.2020.110079>.
- Hu, H., Qi, L., and Chao, X. Physics-informed neural networks (pinns) for computational solid mechanics: Numerical frameworks and applications. *Thin-Walled Structures*, 205:112495, 2024.
- Huang, B. and Wang, J. Applications of physics-informed neural networks in power systems—a review. *IEEE Transactions on Power Systems*, 38(1):572–588, 2022.
- Huang, J., Qiu, R., Wang, J., and Wang, Y. Multi-scale physics-informed neural networks for solving high reynolds number boundary layer flows based on matched asymptotic expansions. *Theoretical and Applied Mechanics Letters*, 14(2):100496, March 2024. ISSN 2095-0349. doi: 10.1016/j.taml.2024.100496.
- Hughes, T. J., Cottrell, J. A., and Bazilevs, Y. Isogeometric analysis: Cad, finite elements, nurbs, exact geometry and mesh refinement. *Computer methods in applied mechanics and engineering*, 194(39-41):4135–4195, 2005.
- Hwang, L. K. Physics-informed machine learning with domain decomposition and global dynamics for three-dimensional intersecting flows. In *The Thirty-ninth Annual Conference on Neural Information Processing Systems*, 2025. URL <https://openreview.net/forum?id=rOuRpOA6pm>.
- Jagtap, A. D., Kharazmi, E., and Karniadakis, G. E. Conservative physics-informed neural networks on discrete domains for conservation laws: Applications to forward and inverse problems. *Computer Methods in Applied Mechanics and Engineering*, 365:113028, June 2020. ISSN 0045-7825. doi: 10.1016/j.cma.2020.113028.
- Jin, X., Cai, S., Li, H., and Karniadakis, G. E. Nsfnets (navier-stokes flow nets): Physics-informed neural networks for the incompressible navier-stokes equations. *Journal of Computational Physics*, 426:109951, February 2021. ISSN 0021-9991. doi: 10.1016/j.jcp.2020.109951. URL <http://dx.doi.org/10.1016/j.jcp.2020.109951>.
- Karniadakis, G. E., Kevrekidis, I. G., Lu, L., Perdikaris, P., Wang, S., and Yang, L. Physics-informed machine learning. *Nature Reviews Physics*, 3(6):422–440, 2021.

- Kharazmi, E., Zhang, Z., and Karniadakis, G. E. Variational physics-informed neural networks for solving partial differential equations. *arXiv preprint arXiv:1912.00873*, 2019.
- Kharazmi, E., Zhang, Z., and Karniadakis, G. E. hp-vpinns: Variational physics-informed neural networks with domain decomposition. *Computer Methods in Applied Mechanics and Engineering*, 374:113547, 2021.
- Krishnapriyan, A., Gholami, A., Zhe, S., Kirby, R., and Mahoney, M. W. Characterizing possible failure modes in physics-informed neural networks. *Advances in neural information processing systems*, 34:26548–26560, 2021.
- Liu, Z., Cai, W., and John Xu, Z.-Q. Multi-scale deep neural network (mscalednn) for solving poisson-boltzmann equation in complex domains. *Communications in Computational Physics*, 28(5):1970–2001, June 2020. ISSN 1991-7120. doi: 10.4208/cicp.oa-2020-0179.
- Lu, L., Meng, X., Mao, Z., and Karniadakis, G. E. Deepxde: A deep learning library for solving differential equations. *SIAM Review*, 63(1):208–228, January 2021. ISSN 1095-7200. doi: 10.1137/19m1274067.
- Maddu, S., Sturm, D., Müller, C. L., and Sbalzarini, I. F. Inverse dirichlet weighting enables reliable training of physics informed neural networks. *Machine Learning: Science and Technology*, 3(1):015026, February 2022. ISSN 2632-2153. doi: 10.1088/2632-2153/ac3712.
- Raissi, M., Perdikaris, P., and Karniadakis, G. E. Physics-informed neural networks: A deep learning framework for solving forward and inverse problems involving nonlinear partial differential equations. *Journal of Computational physics*, 378:686–707, 2019.
- Raissi, M., Yazdani, A., and Karniadakis, G. E. Hidden fluid mechanics: Learning velocity and pressure fields from flow visualizations. *Science*, 367(6481):1026–1030, 2020.
- Slotnick, J. P., Khodadoust, A., Alonso, J., Darmofal, D., Gropp, W., Lurie, E., and Mavriplis, D. J. Cfd vision 2030 study: a path to revolutionary computational aerosciences. Technical report, 2014.
- Tagliasacchi, A., Alhashim, I., Olson, M., and Zhang, H. Mean curvature skeletons. *Comput. Graph. Forum*, 31(5):1735–1744, August 2012. ISSN 0167-7055. doi: 10.1111/j.1467-8659.2012.03178.x. URL <https://doi.org/10.1111/j.1467-8659.2012.03178.x>.
- Tancik, M., Srinivasan, P., Mildenhall, B., Fridovich-Keil, S., Raghavan, N., Singhal, U., Ramamoorthi, R., Barron, J., and Ng, R. Fourier features let networks learn high frequency functions in low dimensional domains. *Advances in neural information processing systems*, 33:7537–7547, 2020.
- Toscano, J. D., Oommen, V., Varghese, A. J., Zou, Z., Ahmadi Daryakenari, N., Wu, C., and Karniadakis, G. E. From pinns to pikans: Recent advances in physics-informed machine learning. *Machine Learning for Computational Science and Engineering*, 1(1):1–43, 2025.
- Versteeg, H. K. *An introduction to computational fluid dynamics the finite volume method, 2/E*. Pearson Education India, 2007.
- Wang, L., Wang, H., Liang, L., Li, J., Zeng, Z., and Liu, Y. Physics-informed neural networks for transcranial ultrasound wave propagation. *Ultrasonics*, 132:107026, 2023.
- Wang, S., Teng, Y., and Perdikaris, P. Understanding and mitigating gradient flow pathologies in physics-informed neural networks. *SIAM Journal on Scientific Computing*, 43(5):A3055–A3081, January 2021a. ISSN 1095-7197. doi: 10.1137/20m1318043.
- Wang, S., Wang, H., and Perdikaris, P. On the eigenvector bias of fourier feature networks: From regression to solving multi-scale pdes with physics-informed neural networks. *Computer Methods in Applied Mechanics and Engineering*, 384:113938, October 2021b. ISSN 0045-7825. doi: 10.1016/j.cma.2021.113938.
- Wang, S., Yu, X., and Perdikaris, P. When and why pinns fail to train: A neural tangent kernel perspective. *Journal of Computational Physics*, 449:110768, January 2022. ISSN 0021-9991. doi: 10.1016/j.jcp.2021.110768.
- Wang, S., Li, B., Chen, Y., and Perdikaris, P. Piratenets: Physics-informed deep learning with residual adaptive networks. *Journal of Machine Learning Research*, 25(402):1–51, 2024. URL <http://jmlr.org/papers/v25/24-0313.html>.
- Wang, S., bhartari, A. K., Li, B., and Perdikaris, P. Gradient alignment in physics-informed neural networks: A second-order optimization perspective. In *The Thirtieth Annual Conference on Neural Information Processing Systems*, 2025a. URL <https://openreview.net/forum?id=iweeV11RHU>.
- Wang, Y., Sun, J., Bai, J., Anitescu, C., Eshaghi, M. S., Zhuang, X., Rabczuk, T., and Liu, Y. Kolmogorov–arnold-informed neural network: A physics-informed deep learning framework for solving forward and inverse problems based on kolmogorov–arnold networks. *Computer Methods in Applied Mechanics and Engineering*, 433:117518, January 2025b. ISSN 0045-7825. doi: 10.1016/j.cma.2024.117518.

- Weng, Y. and Zhou, D. Multiscale physics-informed neural networks for stiff chemical kinetics. *The Journal of Physical Chemistry A*, 126(45):8534–8543, November 2022. ISSN 1520-5215. doi: 10.1021/acs.jpca.2c06513.
- Wu, C., Zhu, M., Tan, Q., Kartha, Y., and Lu, L. A comprehensive study of non-adaptive and residual-based adaptive sampling for physics-informed neural networks. *Computer Methods in Applied Mechanics and Engineering*, 403:115671, January 2023. ISSN 0045-7825. doi: 10.1016/j.cma.2022.115671.
- Wu, H., Luo, H., Ma, Y., Wang, J., and Long, M. Ropinn: Region optimized physics-informed neural networks. *Advances in Neural Information Processing Systems*, 37: 110494–110532, 2024.
- Yao, J., Su, C., Hao, Z., Liu, S., Su, H., and Zhu, J. Multiadam: Parameter-wise scale-invariant optimizer for multiscale training of physics-informed neural networks. In *ICML*, pp. 39702–39721, 2023. URL <https://proceedings.mlr.press/v202/yao23c.html>.
- Yeraneer, K. and Rao, Y. A review of recent investigations on flow and heat transfer enhancement in cooling channels embedded with triply periodic minimal surfaces (tpms). *Energies*, 15(23):8994, 2022.
- Zapf, B., Haubner, J., Kuchta, M., Ringstad, G., Eide, P. K., and Mardal, K.-A. Investigating molecular transport in the human brain from mri with physics-informed neural networks. *Scientific Reports*, 12(1), September 2022. ISSN 2045-2322. doi: 10.1038/s41598-022-19157-w.
- Zhang, W., Pan, H., Lu, L., Duan, X., Yan, X., Wang, R., and Du, Q. Dualms: Implicit dual-channel minimal surface optimization for heat exchanger design. In *Proceedings of the Special Interest Group on Computer Graphics and Interactive Techniques Conference Conference Papers*, SIGGRAPH Conference Papers '25, pp. 1–10. ACM, July 2025. doi: 10.1145/3721238.3730700.

A. Detailed Methodology

A.1. Reynolds number definition.

The nondimensionalization uses a characteristic length scale L_0 and a characteristic velocity scale U_0 , with

$$Re = \frac{U_0 L_0}{\nu}, \quad (19)$$

where ν is the kinematic viscosity. In our setting, we take U_0 as the prescribed inlet mean velocity, and set L_0 to the hydraulic diameter,

$$L_0 := D_h = \frac{4A}{P}, \quad (20)$$

where A is the cross-sectional flow area and P is the corresponding wetted perimeter.

A.2. Constructing and sampling the clipped boundary $\partial V(\mathbf{c}, r)$

For each local integration subdomain $V(\mathbf{c}, r) = B(\mathbf{c}, r) \cap \Omega$, we need to sample points on the clipped boundary $\partial V(\mathbf{c}, r) = \partial(B(\mathbf{c}, r) \cap \Omega)$. The $\partial V(\mathbf{c}, r)$ decomposes into the spherical part and the clipped geometry part:

$$\partial V(\mathbf{c}, r) = \underbrace{(\partial B(\mathbf{c}, r) \cap \Omega)}_{\partial V_{\text{sph}}(\mathbf{c}, r)} \cup \underbrace{(B(\mathbf{c}, r) \cap \partial \Omega)}_{\partial V_{\text{bdry}}(\mathbf{c}, r)}. \quad (21)$$

Accordingly, we construct samples on ∂V_{sph} and ∂V_{bdry} via rejection sampling.

Sphere part $\partial V_{\text{sph}}(\mathbf{c}, r) = \partial B(\mathbf{c}, r) \cap \Omega$. We first draw N_B sampling points $\mathcal{P}_B = \{\mathbf{y}_i\}_{i=1}^{N_B}$ uniformly on the full sphere surface $\partial B(\mathbf{c}, r)$. We then keep the subset that lies inside the domain:

$$\mathcal{P}_{\text{sph}}(\mathbf{c}, r) = \{\mathbf{y} \in \mathcal{P}_B : \mathbf{y} \in \Omega\}. \quad (22)$$

In our implementation, the inside-domain test is computed by the Embree-accelerated containment query in `trimesh` (`mesh.contains`), which performs a standard inside/outside classification for watertight triangle meshes. For any accepted sphere sample $\mathbf{y} \in \mathcal{P}_{\text{sph}}(\mathbf{c}, r)$, the outward unit normal is analytic:

$$\mathbf{n}(\mathbf{y}) = \frac{\mathbf{y} - \mathbf{c}}{\|\mathbf{y} - \mathbf{c}\|_2}. \quad (23)$$

Geometry part $\partial V_{\text{bdry}}(\mathbf{c}, r) = B(\mathbf{c}, r) \cap \partial \Omega$. We represent $\partial \Omega$ as a watertight triangle mesh and draw N_Ω sampling points $\mathcal{P}_\Omega = \{\mathbf{x}_i\}_{i=1}^{N_\Omega}$ approximately uniformly with respect to surface area on $\partial \Omega$. We then keep the subset that lies inside the ball:

$$\mathcal{P}_{\text{bdry}}(\mathbf{c}, r) = \{\mathbf{x} \in \mathcal{P}_\Omega : \|\mathbf{x} - \mathbf{c}\|_2 \leq r\}. \quad (24)$$

For any accepted geometry sample $\mathbf{x} \in \mathcal{P}_{\text{bdry}}(\mathbf{c}, r)$, the outward normal $\mathbf{n}(\mathbf{x})$ is provided by the mesh.

Reuse for Monte Carlo integration. The accepted sample sets $\mathcal{P}_{\text{sph}}(\mathbf{c}, r)$ and $\mathcal{P}_{\text{bdry}}(\mathbf{c}, r)$ are used both for (i) estimating the component areas A_{sph} and A_{bdry} (Appendix A.4) and (ii) evaluating the corresponding surface integrals by Monte Carlo quadrature (Appendix A.3), thereby avoiding additional sampling overhead.

A.3. Monte Carlo estimation of surface integrals.

The weak-form residuals $R_c(\mathbf{c}, r)$ and $\mathbf{R}_m(\mathbf{c}, r)$ involve surface integrals over the boundary $\partial V(\mathbf{c}, r)$. We approximate these integrals via Monte Carlo surface sampling. For any integrand $g(\mathbf{x})$ defined on $\partial V(\mathbf{c}, r)$, we use

$$\oint_{\partial V(\mathbf{c}, r)} g(\mathbf{x}) dS \approx A(\mathbf{c}, r) \cdot \frac{1}{K} \sum_{k=1}^K g(\mathbf{x}_k), \quad (25)$$

where $\{\mathbf{x}_k\}_{k=1}^K$ are samples approximately uniform on $\partial V(\mathbf{c}, r)$, and $A(\mathbf{c}, r) = \int_{\partial V(\mathbf{c}, r)} dS$ is the boundary area. For vector-valued integrands, we apply the estimator component-wise.

In practice, $\partial V(\mathbf{c}, r)$ can be decomposed into two components:

$$\partial V(\mathbf{c}, r) = \partial V_{\text{sph}} \cup \partial V_{\text{bdry}}, \quad (26)$$

with $\partial V_{\text{sph}} = \partial B(\mathbf{c}, r) \cap \Omega$ and $\partial V_{\text{bdry}} = B(\mathbf{c}, r) \cap \partial \Omega$. We sample points on each component and combine them with area weights:

$$\oint_{\partial V} g dS \approx A_{\text{sph}} \cdot \frac{1}{K_{\text{sph}}} \sum_{k=1}^{K_{\text{sph}}} g(\mathbf{x}_k^{\text{sph}}) + A_{\text{bdry}} \cdot \frac{1}{K_{\text{bdry}}} \sum_{k=1}^{K_{\text{bdry}}} g(\mathbf{x}_k^{\text{bdry}}), \quad (27)$$

where $K_{\text{sph}} + K_{\text{bdry}} = K$ and $A_{\text{sph}} + A_{\text{bdry}} = A(\mathbf{c}, r)$. On ∂V_{sph} , the outward unit normal is analytic: $\mathbf{n} = (\mathbf{x} - \mathbf{c}) / \|\mathbf{x} - \mathbf{c}\|$. On ∂V_{bdry} , \mathbf{n} is provided by the geometry. The areas A_{sph} and A_{bdry} are estimated by rejection sampling on the sphere and the geometry surface, respectively (Appendix A.4).

Applying the Monte Carlo estimator to our weak-form residuals amounts to sampling the boundary flux integrands on $\partial V(\mathbf{c}, r)$.

For the continuity residual in Eq. (8), the scalar integrand is

$$g_c(\mathbf{x}) = \mathbf{u}_\theta(\mathbf{x}) \cdot \mathbf{n}(\mathbf{x}) \in \mathbb{R}. \quad (28)$$

For the momentum residual in Eq. (12), the integrand is the vector

$$\mathbf{g}_m(\mathbf{x}) = \mathbf{F}_\theta(\mathbf{x})\mathbf{n}(\mathbf{x}) \in \mathbb{R}^3, \quad (29)$$

where $\mathbf{F}_\theta = \mathbf{u}_\theta \otimes \mathbf{u}_\theta + p_\theta \mathbf{I} - \frac{1}{Re} \nabla \mathbf{u}_\theta$ is the network-induced flux tensor, and $\mathbf{u}_\theta, p_\theta$ are predicted by the network f_θ .

A.4. Estimating A_{sph} and A_{bdry} by Rejection Sampling

Recall the boundary decomposition $\partial V(\mathbf{c}, r) = \partial V_{\text{sph}} \cup \partial V_{\text{bdry}}$, where $\partial V_{\text{sph}} = \partial B(\mathbf{c}, r) \cap \Omega$ and $\partial V_{\text{bdry}} = B(\mathbf{c}, r) \cap \partial \Omega$. To combine Monte Carlo estimates from the two components, we require the component areas A_{sph} and A_{bdry} . We estimate them via rejection sampling using simple membership tests.

Spherical component area A_{sph} . Following Appendix A.2, we draw N_B sampling points $\mathcal{P}_B = \{\mathbf{y}_i\}_{i=1}^{N_B}$ uniformly on $\partial B(\mathbf{c}, r)$ and obtain the accepted subset $\mathcal{P}_{\text{sph}}(\mathbf{c}, r) = \{\mathbf{x}_k^{\text{sph}}\}_{k=1}^{K_{\text{sph}}}$ via the inside-domain test in Eq. (22). The acceptance ratio is estimated as

$$\hat{p}_{\text{sph}} = \frac{K_{\text{sph}}}{N_B} = \frac{1}{N_B} \sum_{i=1}^{N_B} \mathbb{I}[\mathbf{y}_i \in \Omega]. \quad (30)$$

Since the surface area of $\partial B(\mathbf{c}, r)$ equals $4\pi r^2$, we estimate

$$\hat{A}_{\text{sph}} = 4\pi r^2 \cdot \hat{p}_{\text{sph}}. \quad (31)$$

Boundary component area A_{bdry} . Following Appendix A.2, we draw N_Ω sampling points $\mathcal{P}_\Omega = \{\mathbf{z}_i\}_{i=1}^{N_\Omega}$ approximately uniformly (w.r.t. surface area) on $\partial \Omega$ and obtain the accepted subset $\mathcal{P}_{\text{bdry}}(\mathbf{c}, r) = \{\mathbf{x}_k^{\text{bdry}}\}_{k=1}^{K_{\text{bdry}}}$ via the inside-ball test in Eq. (24). The acceptance ratio is estimated as

$$\hat{p}_{\text{bdry}} = \frac{K_{\text{bdry}}}{N_\Omega} = \frac{1}{N_\Omega} \sum_{i=1}^{N_\Omega} \mathbb{I}[\|\mathbf{z}_i - \mathbf{c}\|_2 \leq r]. \quad (32)$$

Let $A(\partial \Omega)$ denote the total surface area of $\partial \Omega$. We estimate the clipped boundary area as

$$\hat{A}_{\text{bdry}} = A(\partial \Omega) \cdot \hat{p}_{\text{bdry}}. \quad (33)$$

Remarks. (i) The estimators above are consistent under area-uniform sampling on the corresponding surfaces. (ii) In our implementation, the same samples used to estimate \hat{A}_{sph} and \hat{A}_{bdry} can also be reused for evaluating surface integrals on each component, thereby avoiding additional sampling overhead.

A.5. Radius selection.

Our goal is to choose the three radii (r_L, r_M, r_S) in a geometry-aware and reproducible way, so that (i) large subdomains provide long-range coupling, (ii) medium subdomains match the channel scale along the skeleton, and (iii) small subdomains refine local geometric details while keeping the Monte Carlo estimator stable.

Geometry scales. Let the axis-aligned bounding box of Ω have side lengths $(\Delta x, \Delta y, \Delta z)$. Denote the sorted side lengths by $d_1 \leq d_2 \leq d_3$. To characterize the channel thickness, we use the distance-to-boundary (local inscribed radius)

$$\rho(\mathbf{x}) = \text{dist}(\mathbf{x}, \partial\Omega), \quad \mathbf{x} \in \Omega, \quad (34)$$

which is evaluated either from a signed distance field (SDF) or nearest-boundary queries. We compute $\rho(\mathbf{c})$ on skeleton centers $\mathbf{c} \in \mathcal{C}_M$ to obtain a robust estimate of the ‘‘wide-channel’’ scale:

$$\hat{\rho}_M = Q_{0.9}(\{\rho(\mathbf{c})\}_{\mathbf{c} \in \mathcal{C}_M}), \quad (35)$$

where $Q_{0.9}(\cdot)$ denotes the 90% quantile. Using a high quantile behaves similarly to the maximum channel radius, but is more robust to outliers.

Radius rules. We set the radii by the following rules:

$$r_L = \alpha_L \cdot \frac{1}{2} \sqrt{d_1^2 + d_2^2}, \quad (36)$$

$$r_M = \alpha_M \cdot \hat{\rho}_M, \quad (37)$$

$$r_S = \beta \cdot r_M. \quad (38)$$

Eq. (36) chooses r_L as an inflated circumradius of the rectangle formed by the two smallest box extents, which avoids overly large subdomains in highly anisotropic geometries while still enabling domain-level coverage and long-range flux coupling. Eq. (37) ties r_M to the channel thickness along the skeleton so that skeleton-centered subdomains cover the transport pathways. Eq. (38) sets a nested refinement scale relative to the medium one.

In our experiments, we use fixed coefficients across all experiments:

$$\alpha_L = \alpha_M = 1.4, \quad \beta = 0.5. \quad (39)$$

Here $\alpha_L, \alpha_M > 1$ are mild inflation factors that increase overlap and compensate for geometric truncation, and β controls the refinement ratio between medium and small scales. We found performance to be insensitive to moderate changes of these coefficients due to the complementary multi-scale coverage.

A.6. Boundary Conditions.

We enforce Dirichlet-type inlet velocity, outlet pressure, and no-slip wall conditions using mean-squared penalty terms on boundary point sets. Let $\mathcal{X}_{bc} \subset \partial\Omega$ denote the sampled boundary points. We partition it according to boundary types:

$$\mathcal{X}_{in} = \mathcal{X}_{bc} \cap \Gamma_{in}, \quad \mathcal{X}_{out} = \mathcal{X}_{bc} \cap \Gamma_{out}, \quad \mathcal{X}_w = \mathcal{X}_{bc} \cap \Gamma_w. \quad (40)$$

For each $\mathbf{x} \in \mathcal{X}_{bc}$, the network prediction is $(\mathbf{u}_\theta(\mathbf{x}), p_\theta(\mathbf{x})) = f_\theta(\mathbf{x})$. The prescribed boundary values are given by $\mathbf{u}_{in}(\mathbf{x})$ on Γ_{in} and $p_{out}(\mathbf{x})$ on Γ_{out} .

The inlet-velocity penalty is

$$\mathcal{L}_{in} = \frac{1}{|\mathcal{X}_{in}|} \sum_{\mathbf{x} \in \mathcal{X}_{in}} \|\mathbf{u}_\theta(\mathbf{x}) - \mathbf{u}_{in}(\mathbf{x})\|_2^2. \quad (41)$$

The outlet-pressure penalty is

$$\mathcal{L}_{out} = \frac{1}{|\mathcal{X}_{out}|} \sum_{\mathbf{x} \in \mathcal{X}_{out}} |p_\theta(\mathbf{x}) - p_{out}(\mathbf{x})|^2. \quad (42)$$

The no-slip wall penalty is

$$\mathcal{L}_w = \frac{1}{|\mathcal{X}_w|} \sum_{\mathbf{x} \in \mathcal{X}_w} \|\mathbf{u}_\theta(\mathbf{x})\|_2^2. \quad (43)$$

Finally, the boundary-condition loss used in the main objective is

$$\mathcal{L}_{bc} = \lambda_{in} \mathcal{L}_{in} + \lambda_{out} \mathcal{L}_{out} + \lambda_w \mathcal{L}_w. \quad (44)$$

B. Detailed Experimental Setup and Ground Truth Generation

In this section, we provide the precise definitions of the geometric configurations, physical parameters, and numerical protocols used to generate the high-fidelity ground truth data via Ansys CFX.

B.1. Geometric Definitions of TPMS Structures

The porous media geometries used in this study are defined by Triply Periodic Minimal Surfaces (TPMS). The implicit level-set equations approximation for the Primitive (P), Gyroid (G), Diamond (D), and IWP structures are given as follows:

$$\Phi_P(x, y, z) = \cos(2\pi x) + \cos(2\pi y) + \cos(2\pi z) = 0, \quad (45)$$

$$\Phi_G(x, y, z) = \sin(2\pi x) \cos(2\pi y) + \sin(2\pi y) \cos(2\pi z) + \sin(2\pi z) \cos(2\pi x) = 0, \quad (46)$$

$$\begin{aligned} \Phi_D(x, y, z) = & \sin(2\pi x) \sin(2\pi y) \sin(2\pi z) + \sin(2\pi x) \cos(2\pi y) \cos(2\pi z) \\ & + \cos(2\pi x) \sin(2\pi y) \cos(2\pi z) + \cos(2\pi x) \cos(2\pi y) \sin(2\pi z) = 0, \end{aligned} \quad (47)$$

$$\begin{aligned} \Phi_{IWP}(x, y, z) = & 2(\cos(2\pi x) \cos(2\pi y) + \cos(2\pi y) \cos(2\pi z) + \cos(2\pi z) \cos(2\pi x)) \\ & - (\cos(4\pi x) + \cos(4\pi y) + \cos(4\pi z)) = 0. \end{aligned} \quad (48)$$

Fig. 8 visualizes the four TPMS geometries and our domain construction: we tile five unit cells along the streamwise x -direction, resulting in $\Omega = [0, 5L] \times [0, L] \times [0, L]$ with unit-cell length $L = 1$.

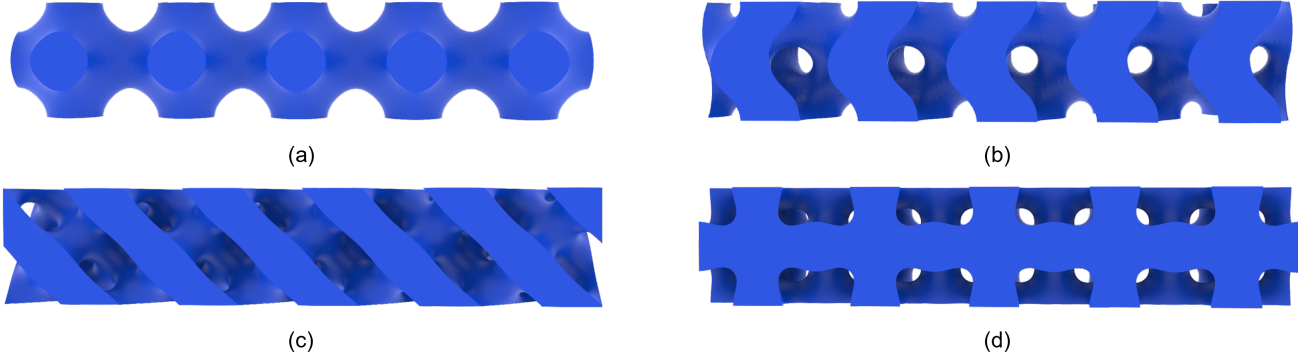


Figure 8. TPMS heat-exchanger channels used in our experiments. The domain is constructed by tiling five unit cells along the streamwise x -direction, yielding $\Omega = [0, 5L] \times [0, L] \times [0, L]$ with unit-cell length $L = 1$. Panels (a)–(d) show *Primitive (P)*, *Gyroid (G)*, *Diamond (D)*, and *IWP*, respectively.

B.2. Simulation Settings and Numerical Solver Configuration

Governing Equations and Boundary Conditions We simulate the steady-state flow of an incompressible Newtonian fluid governed by the Navier-Stokes equations:

$$\nabla \cdot \mathbf{u} = 0, \quad (49)$$

$$(\mathbf{u} \cdot \nabla) \mathbf{u} = -\frac{1}{\rho} \nabla p + \nu \nabla^2 \mathbf{u}, \quad (50)$$

where \mathbf{u} is the velocity vector, p is pressure, ρ is density, and ν is kinematic viscosity. The simulation is characterized by a Reynolds number $Re = \frac{U_{in} L}{\nu} = 100$, ensuring the flow remains in the laminar regime.

Numerical Solver Configuration High-fidelity ground truth data were generated using Ansys CFX, a commercial CFD solver based on the finite volume method (FVM). The specific solver settings are detailed as follows:

- **Mesh Generation:** An unstructured tetrahedral mesh was generated to discretize the computational domain. To accurately capture the boundary layer gradients, prismatic inflation layers were applied near the wall surfaces. The

boundary layer mesh consisted of 5 layers with a first layer height of 0.002 and a growth rate of 1.2. A global element size of 0.02 was applied, with a refined maximum size of 0.01 near the boundaries. This configuration resulted in a high-resolution grid containing approximately 10^7 (tens of millions) elements.

- **Discretization Scheme:** A High-Resolution advection scheme was employed for the spatial discretization of momentum and mass equations to ensure both numerical stability and second-order equivalent accuracy.
- **Convergence Criteria:** The simulations were subjected to strict convergence criteria. The iterative process was terminated only when the root-mean-square (RMS) residuals for all governing equations dropped below 1×10^{-8} , ensuring a fully converged and high-fidelity solution.
- **Inlet/Outlet Extensions:** Straight pipe extensions were added at both the inlet and outlet. The inlet extension ensured a developed inflow before entering the TPMS region, while the outlet extension minimized outlet boundary effects and prevented backflow/recirculation near the outlet from contaminating the flow in the TPMS region. The extension length was set to three TPMS unit-cell lengths.

C. Network Architecture and Hyperparameter Values

In this section, we provide the formal definition of the neural network architecture, evaluate the impact of different positional encoding strategies, and detail the hyperparameter configurations to facilitate reproducibility.

C.1. Network Architecture

The proposed physics-informed framework employs a fully connected feed-forward neural network (MLP) augmented with a Fourier feature mapping layer. This architecture is designed to mitigate the spectral bias inherent in standard coordinate-based MLPs.

Fourier Feature Embedding. Let $\mathbf{x} \in \Omega \subset \mathbb{R}^3$ denote the input spatial coordinates. We project \mathbf{x} into a high-dimensional feature space using a deterministic Fourier mapping $\gamma : \mathbb{R}^3 \rightarrow \mathbb{R}^{2m}$. Unlike standard Random Fourier Features (RFF) where frequencies are sampled from a Gaussian distribution, we employ linearly spaced frequency bands to ensure uniform spectral coverage within the target bandwidth. The embedding is defined as:

$$\gamma(\mathbf{x}) = [\sin(2\pi\mathbf{B}\mathbf{x}), \cos(2\pi\mathbf{B}\mathbf{x})]^\top, \quad (51)$$

where $\mathbf{B} \in \mathbb{R}^{m \times 3}$ represents the frequency matrix. The frequencies are initialized linearly within the range $[f_{min}, f_{max}]$ to capture multi-scale flow features. In our final model, we set the embedding dimension to $2m = 60$.

Backbone and Output Layers. The embedded features $\gamma(\mathbf{x})$ serve as the input to an MLP comprising D hidden layers with W neurons per layer. We utilize the Tanh activation function $\sigma(\cdot)$ to guarantee the higher-order differentiability required for computing PDE derivatives. The forward propagation is given by:

$$\mathbf{h}_0 = \gamma(\mathbf{x}), \quad (52)$$

$$\mathbf{h}_k = \sigma(\mathbf{W}_k \mathbf{h}_{k-1} + \mathbf{b}_k), \quad k = 1, \dots, D. \quad (53)$$

The final output layer projects the hidden features \mathbf{h}_D to the physical variables of interest, namely the velocity vector $\mathbf{u} = (u, v, w)$ and pressure p , via a linear transformation without activation:

$$[\mathbf{u}, p] = \mathbf{W}_{out} \mathbf{h}_D + \mathbf{b}_{out}. \quad (54)$$

Network weights are initialized using the Glorot scheme.

C.2. Position Encoding Comparison

To identify the optimal spectral mapping strategy for flow fields, we conducted a systematic evaluation of four embedding configurations on the Gyroid geometry ($Re = 100$):

- (i) **Standard MLP:** Direct coordinate input without embedding ($\gamma(\mathbf{x}) = \mathbf{x}$), serving as the baseline.

- (ii) **Gaussian Random Fourier Feature:** Frequencies sampled from a Gaussian distribution $\mathbf{B} \sim \mathcal{N}(0, \sigma^2)$, introducing stochasticity.
- (iii) **Exponential Fourier Feature:** Deterministic frequencies spaced geometrically (i.e., $f_k = \alpha^k$), a standard setting in neural rendering to capture multi-resolution features.
- (iv) **Linear Fourier Feature (Ours):** Deterministic frequencies spaced linearly within the target bandwidth $[f_{min}, f_{max}]$, ensuring uniform spectral coverage.

Quantitative Results. Table 4 summarizes the convergence performance. The Standard MLP suffers from spectral bias, failing to resolve sharp boundary layers. Gaussian Random Fourier Feature improves accuracy but exhibits variance due to random sampling. Exponential Fourier Feature effectively captures global structures but empirically struggles with mid-frequency transition regions in our fluid benchmarks. In contrast, Linear Fourier Feature achieves the lowest absolute ℓ_2 error, suggesting that uniform spectral coverage is critical for resolving the continuous multi-scale features inherent in Navier-Stokes dynamics.

Table 4. Comparative analysis of positional encoding strategies. **Linear-FF** demonstrates superior convergence and final accuracy compared to RFF and Exponential FF mappings.

Encoding Strategy	Type	Rel. ℓ_2 on $ \mathbf{u} \downarrow$	Rel. ℓ_2 on $p \downarrow$
Standard MLP	Identity	70.47%	33.93%
Gaussian RFF	Stochastic	18.64%	4.74%
Exponential FF	Deterministic	6.92%	30.73%
Linear-FF (Ours)	Deterministic	3.76%	5.36%

C.3. Hyperparameter Values

We summarize all hyperparameters used in our experiments for reproducibility, including boundary-condition sampling, strong-form collocation sampling, local subdomain sampling (large/medium/small balls), Monte Carlo surface sampling on $\partial V(\mathbf{c}, r)$, optimization, and loss weights in Table 5.

All experiments in Table 1 were conducted on a single NVIDIA A40 GPU using PyTorch, and we use a fully-connected MLP to parameterize the solution fields. Given an input 3D coordinate $\mathbf{x} \in \mathbb{R}^3$, we first apply a linear Fourier feature mapping to obtain a 60-dimensional embedding $\phi(\mathbf{x}) \in \mathbb{R}^{60}$ with frequencies bounded in $[1, 2.5]$. The embedding is then fed into an MLP with 5 hidden layers of width 256. The network outputs a 4-dimensional vector $\hat{\mathbf{y}}(\mathbf{x}) = [u(\mathbf{x}), v(\mathbf{x}), w(\mathbf{x}), p(\mathbf{x})]$, corresponding to the three velocity components and pressure.

D. More Experiments Results

D.1. Longitudinal Flow Fidelity

To qualitatively assess how well each method preserves the streamwise flow evolution from inlet to outlet, we visualize a longitudinal mid-plane slice in the Gyroid geometry. Specifically, for the 5-period domain $\Omega = [0, 5] \times [0, 1] \times [0, 1]$, we render the streamwise velocity component $u_x(\mathbf{x})$ on the plane

$$\Pi_z = \{(x, y, z) \in \Omega : z = 0.5\}. \tag{55}$$

This plane spans the full streamwise extent ($x \in [0, 5]$) and provides a compact view of how the flow develops along tortuous passages. Figure 9 compares the resulting longitudinal slices across different methods.

D.2. Local Flow Fidelity

In the main paper, due to space constraints, we only visualize the *scalar* velocity field for competing methods, while omitting the component-wise behaviors. However, matching $|\mathbf{u}|$ alone can hide important directional errors, such as spurious cross-flow, incorrect recirculation orientation, or component-wise bias. To provide a more fine-grained qualitative assessment, we further visualize the three velocity components $\mathbf{u} = (u, v, w)$ for all methods on the same set of slices. Specifically, Figures 10, 11, 12, 13, and 14 correspond to PINN-PE, RoPINN, CoPINN, MDPINN-GD, and MUSA-PINN, respectively, comparing the velocity at $x = 0.5$ with the ground truth.

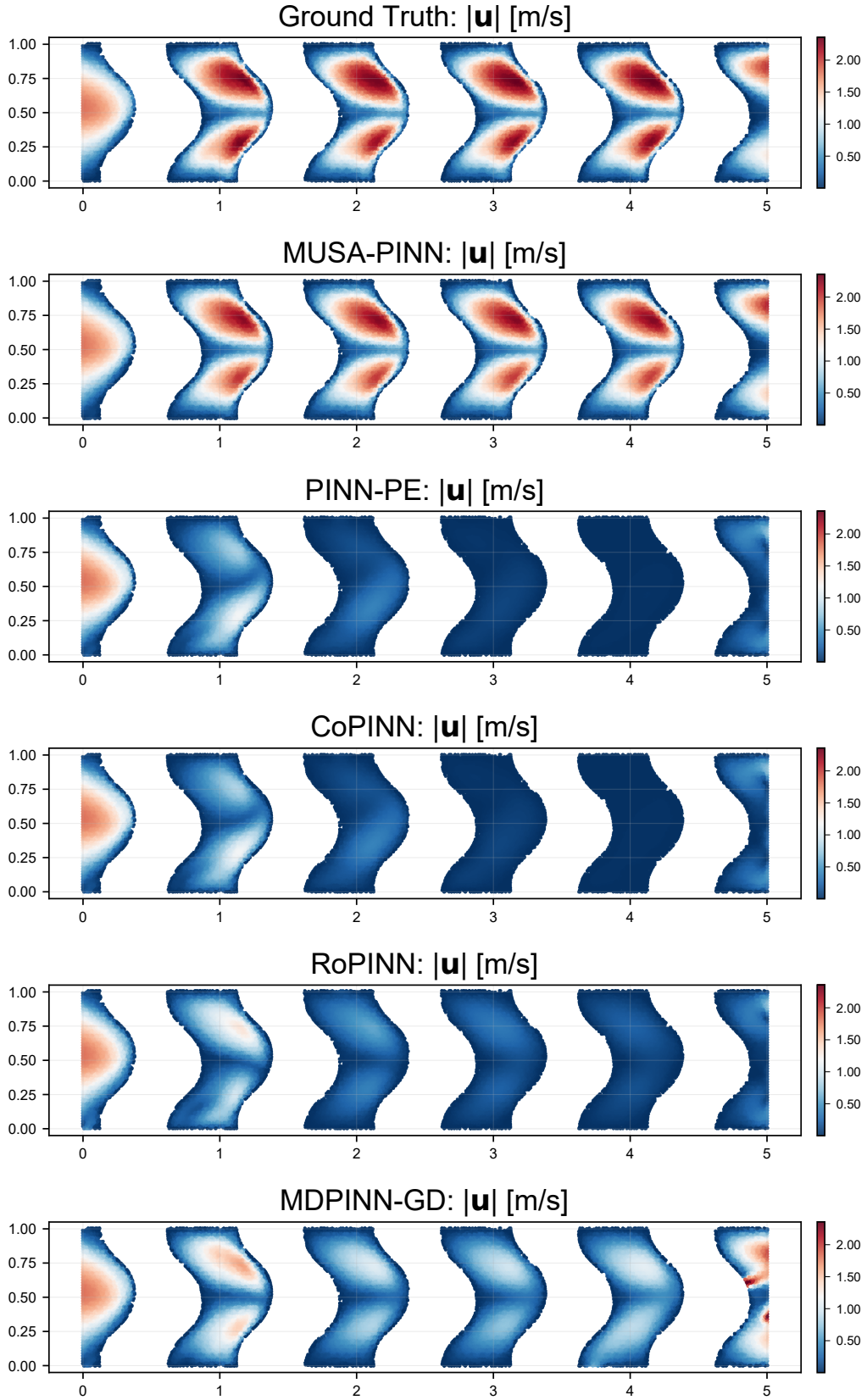


Figure 9. Local flow fidelity in the Gyroid geometry.

Table 5. **Training hyperparameters for MUSA-PINN.** Numbers of boundary-condition samples and interior collocation points for strong-form residuals, multi-scale spherical subdomain configuration $(N_L, N_M, N_S; r_L, r_M, r_S)$, and optimization settings including the two-stage schedule (T_{switch}) and loss weights.

Item	Value
Inlet samples $ \mathcal{X}_{in} $	1000
Outlet samples $ \mathcal{X}_{out} $	1000
Wall (no-slip) samples $ \mathcal{X}_w $	10000
Interior PDE collocation points	250000
Numbers of Large subdomains N_L	40
Numbers of Medium subdomains N_M	200
Numbers of Small subdomains N_S	500
Large-ball radius r_L	1.0
Medium-ball radius r_M	0.5
Small-ball radius r_S	0.25
Optimizer	SOAP
Learning rate (stage 1)	1e-3
Learning rate (stage 2)	1e-6
Total epoch	9000
Stage transition T_{switch}	7000
Inlet BC weight λ_{in}	10
Outlet BC weight λ_{out}	10
No-slip wall BC weight λ_w	10
Strong-form continuity weight λ_c	10
Strong-form momentum weight λ_m	0.1
Weak-form continuity (large) weight λ_c^L	100
Weak-form continuity (medium) weight λ_c^M	100
Weak-form continuity (small) weight λ_c^S	100
Weak-form momentum (large) weight λ_m^L	4
Weak-form momentum (medium) weight λ_m^M	25
Weak-form momentum (small) weight λ_m^S	100

D.3. Training time

To provide a fair and reproducible comparison of computational overhead, we report both wall-clock training time for all methods in Table 6.

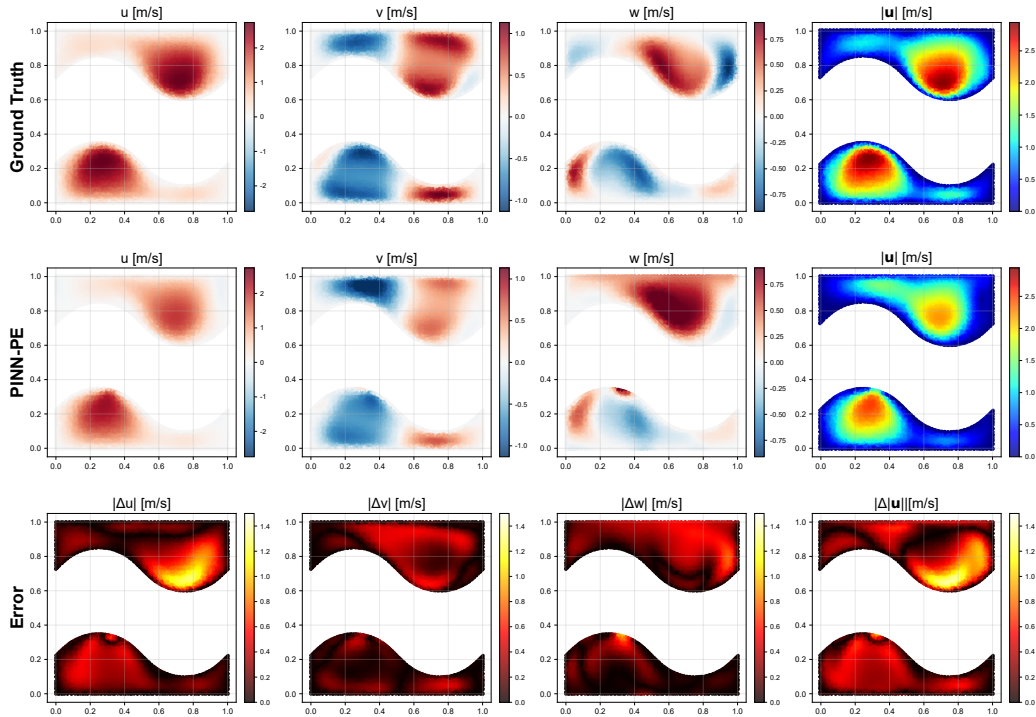


Figure 10. Local flow fidelity at $x = 0.5$ (PINN-PE). Component-wise velocity slices (u, v, w) predicted by PINN-PE compared with the ground truth (GT) on the plane $x = 0.5$.

Table 6. Efficiency comparison. Convergence iterations and training time.

Method	Conv. iters	Time (h)
PINN-PE	15000	10.22
RoPINN	7500	12.35
CoPINN	15000	10.256
MDPINN-GD	45000	38.37
MUSA-PINN (Stage 1)	7000	7.05
MUSA-PINN (Stage 2)	2000	18.79

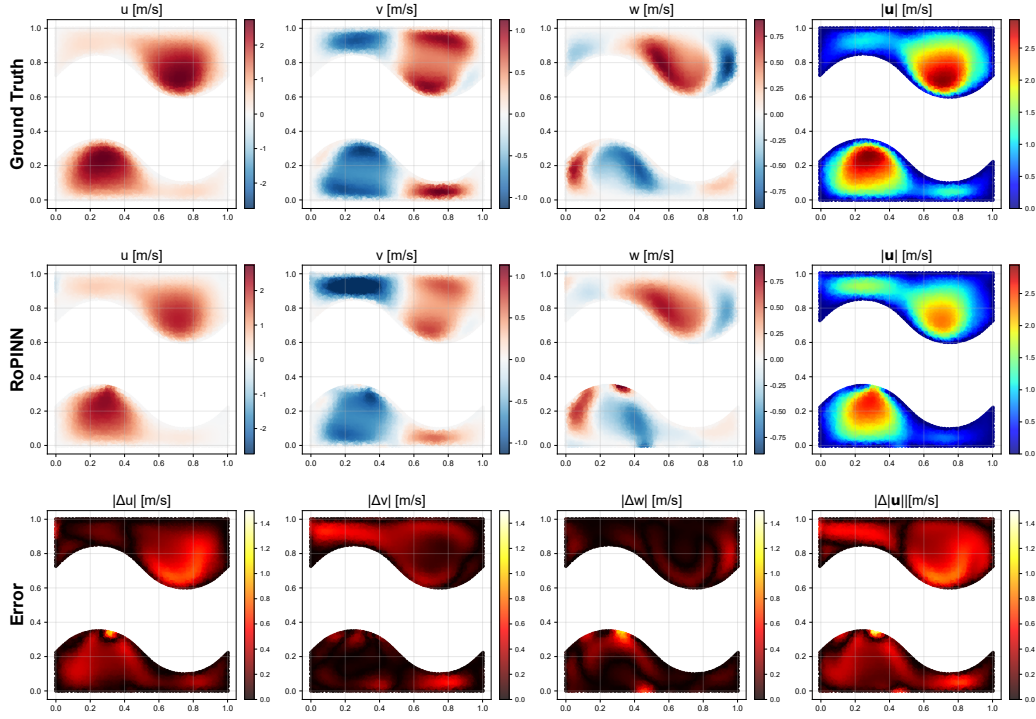


Figure 11. Local flow fidelity at $x = 0.5$ (RoPINN). Component-wise velocity slices (u, v, w) predicted by RoPINN compared with the ground truth (GT) on the plane $x = 0.5$.

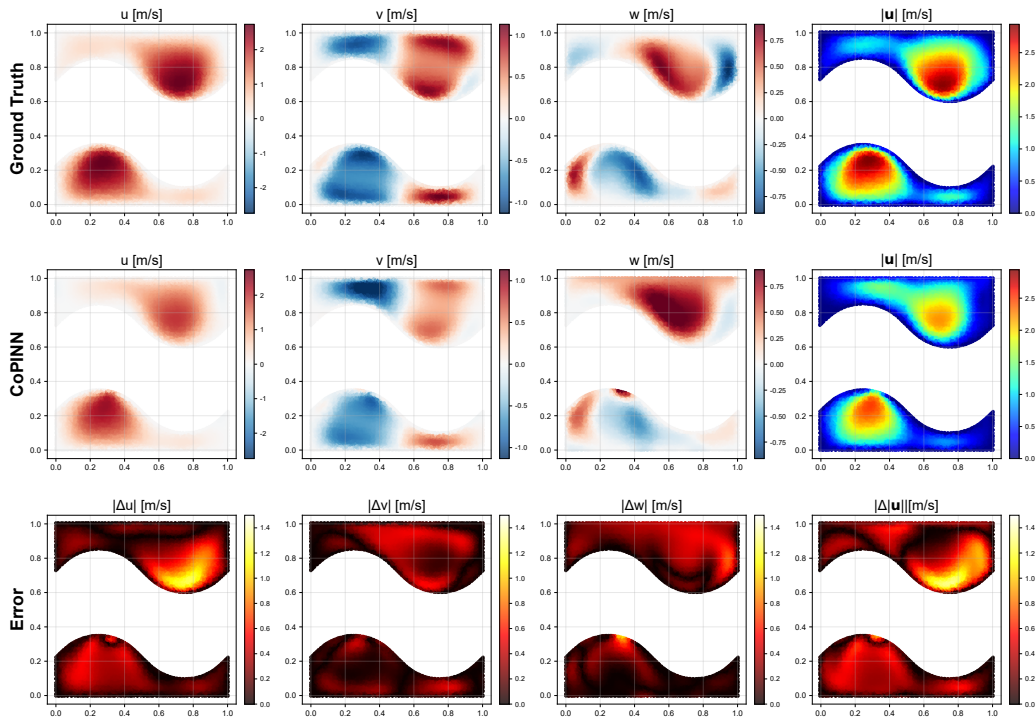


Figure 12. Local flow fidelity at $x = 0.5$ (CoPINN). Component-wise velocity slices (u, v, w) predicted by CoPINN compared with the ground truth (GT) on the plane $x = 0.5$.

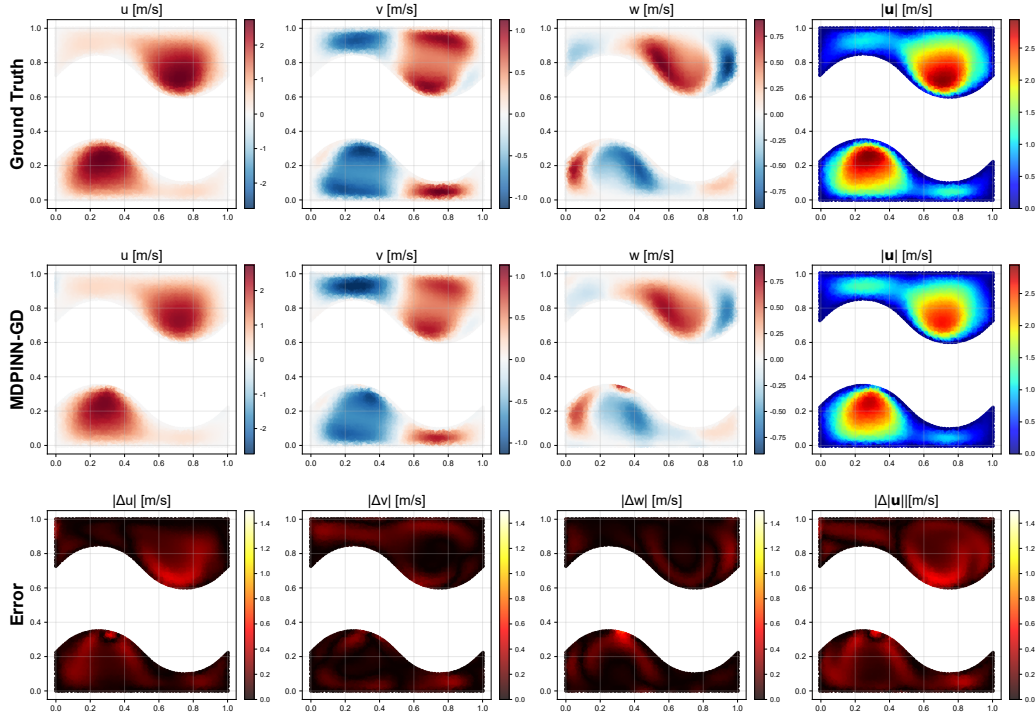


Figure 13. **Local flow fidelity at $x = 0.5$ (MDPINN-GD).** Component-wise velocity slices (u, v, w) predicted by MDPINN-GD compared with the ground truth (GT) on the plane $x = 0.5$.

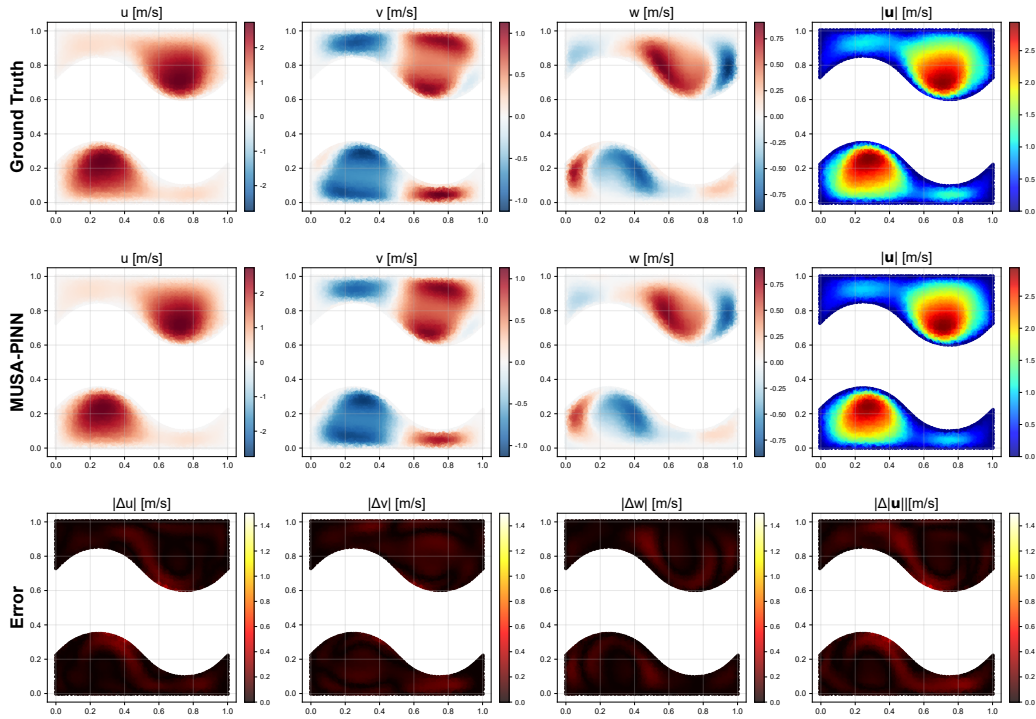


Figure 14. **Local flow fidelity at $x = 0.5$ (MUSA-PINN).** Component-wise velocity slices (u, v, w) predicted by MUSA-PINN compared with the ground truth (GT) on the plane $x = 0.5$.